Activation Energies in MoSi/Al Superconducting Nanowire Single-Photon Detectors

D. Salvoni,[1] M. Ejrnaes,[2] A. Gaggero,[3] F. Mattioli,[3] F. Martini,[3] H.G. Ahmad,[1,4] L. Di Palma,[1] R. Satariano,[1] X.Y. Yang,[5] L. You,[5] F. Tafuri,[1] G.P. Pepe,[1] D. Massarotti,[6] D. Montemurro,[1] and L. Parlato[1,2,*]

[1] *Dip. di Fisica "E. Pancini", Università degli Studi di Napoli Federico II, I-80125 Napoli, Italy*

[2] *CNR-SPIN Institute of Superconductors, Innovative Materials and Devices, I-80078 Pozzuoli, Italy*

[3] *CNR, Institute for Photonics and Nanotechnologies, I-00156 Rome, Italy*

[4] *Seeqc, Strada Comunale Cinthia, I-80125 Napoli, Italy*

[5] *State Key Laboratory of Functional Materials for Informatics, Shanghai Institute of Microsystem and Information Technology (SIMIT), Chinese Academy of Sciences, 865 Changning Road, Shanghai 200050, China*

[6] *Dip. di Ingegneria Elettrica e delle Tecnologie dell'Informazione, Università degli Studi di Napoli Federico II, I-80125 Napoli, Italy*

(Received 31 December 2021; revised 28 February 2022; accepted 26 April 2022; published 5 July 2022)

Superconducting nanowire single-photon detectors (SNSPDs) are receiving the interest of the scientific and industrial communities due to their unparallel high performances in the infrared. However, even though the fabrication process permits the achievement of about 98% efficiency and less than 1 cps dark-count rate, the physical mechanism inducing the detection remains unclear. It is clear however that normal core vortices play a crucial role. In this work we investigate the role of vortices in two-dimensional (2D) molybdenum silicide SNSPDs of different widths covered with an Al layer through the analysis of the switching current distributions from the superconducting to resistive regime, in a wide interval of temperatures from 4.5 K down to 10 mK. This analysis provides the energy scales of different mechanisms that are responsible for fluctuations and dark counts in SNSPDs. We consider two models based on vortices, the unbinding of vortex-antivortex pairs (VAPs) and vortices hopping over the edge barrier (VH) and we underline the differences among different devices made by different materials. We also estimate the energy scales of similar Nb-Ti-N and NbN devices and compare the results. The lower activation energies obtained for MoSi/Al devices, explain the peculiarity of this material to work at longer wavelengths with a higher quantum detection efficiency.

DOI: 10.1103/PhysRevApplied.18.014006

I. INTRODUCTION

Superconducting nanowire single-photon detectors (SNSPDs) consist of an ultrathin (typically a few nm) superconducting nanowire 50–200 nm wide, folded in a meander geometry [1]. These devices find application in many fields, spanning from single-photon source characterization to optical communication, quantum cryptography, and remote sensing [2–4]. The operating principle of a SNSPD is based on the formation of a normal *hotspot* region in the superconducting strip after the photon absorption, which produces a voltage pulse [1]. Besides voltage pulses due to the single-photon detection, a SNSPD might also generate spontaneous transitions, also resulting in transient voltage pulses, generally known as dark counts [1]. A deeper understanding of the physical mechanism of the spontaneous fluctuation events generating the dark counts, can be very relevant to reduce the SNSPDs' dark-count rate (DCR) and to support an *extended* hotspot model.

The hotspot model is supported by several experimental observations, such as the linear photon energy-current bias relation and the observed linear dependence of the threshold on the width, w, and thickness, d, of the nanowire [5], and it provides a reasonable description of the dependence on the material parameters [6,7]. However, it does not explain the position dependence of the threshold current and the slow decreasing of the count rate when the bias current is reduced before the exponential behavior appears, which could be ascribed to fluctuations [5]. The present literature favors the theory that assigns a more relevant role to magnetic vortices moving across the width of a superconducting strip [8,9], either vortex-antivortex

*Corresponding author. lparlato@unina.it

pairs (VAP) or single vortices overcoming the barrier at opposite edges of the stripe, a mechanism called vortex hopping (VH) [10,11]. Both VAP and VH are present in dirty type-II superconductors even in zero magnetic field and they can affect, besides the DCR, also the photodetection in SNSPDs [12].

The investigation of the fluctuations in two-dimensional (2D) superconducting nanowires of d much smaller than the London penetration depth, λ_L, and w much smaller than the Pearl length, $\Lambda = 2\lambda_L^2/d \gg w$, has been extensively discussed in the context of the Berezinsky-Kosterlitz-Thouless (BKT) transition [13] and a deep study of 2D fluctuations in SNSPDs can be performed through the analysis of the switching current distributions [14] from the superconducting to the resistive regime in a wide range of temperatures [15,16]. In this work, we use this tool to study the dark counts in a 9-nm-thick MoSi SNSPD covered with a very thin (2 nm) layer of aluminum, which was previously demonstrated to operate as a single-photon detector at $\lambda = 1550$ nm [17]. It emerges that these measurements are a powerful tool to investigate and quantify the role of the vortices in 2D structures. By the experimental dependences of the switching rates on the bias current, temperature and width of the nanowire, it is possible to calculate the relevant parameters in the framework of VAP and VH theoretical models. Indeed, we quantify the energy scales of the fluctuation phenomena and the maximum detectable wavelength. The estimated values, that we obtain, are larger than what the simple hotspot model predicts for the maximum detectable wavelength, λ_{max}, $\lambda_{max} \sim hc/(N_0\Delta^2 wd\sqrt{(D\tau_{th})(1-I_b/I_c)})$ [6], where Δ, N_0, τ_{th}, D, I_b, and I_c are the superconductor gap, the density of states at the Fermi level, the electron thermalization time, the electron diffusivity, the bias current, and the critical current, respectively. We also define Planck's constant, h, and the speed of light, c.

This paper is organized as follows: in Sec. II A we describe the fabrication and characterization details, in Sec. II B we report on the measurements of the fluctuation rates versus the bias current and temperature, in Sec. III we present the results in the framework of VAP and VH theoretical models. In Sec. IV we give a comparison of the energy scales for different materials and geometries and all the results are summarized in Sec. V.

II. EXPERIMENT

A. Sample fabrication

$Mo_{0.70}Si_{0.30}$ films 9 nm thick are grown on Si (100)/SiO_2 (250 nm) substrates by UHV ($P_{base} = 10^{-7}$ Torr) dc diode magnetron sputtering by using an alloy target at room temperature in an Ar pressure of 2.46 mTorr, at a deposition rate of 0.2 nm/s. By energy dispersive x-ray analysis we can estimate that the final stoichiometry is reliable within a factor of 5%. In the same vacuum chamber, we deposit 2-nm Al thin film in an Ar pressure of 1.50 mTorr at a rate of 0.2 nm/s to protect the superconducting material during the patterning and prevent its oxidation [17]. Indeed, when the Al overlayer is used, we observe an increase of the critical temperature, T_c, of the as-grown MoSi films from $T_c^{MoSi} = 5.3$ K to $T_c^{MoSi/Al} = 6.1$ K, and also that the critical current density, J_c, increases about a factor of 3 as also reported in the literature in the presence of a normal layer [18,19]. The thin films are then patterned by combining an electron-beam lithography (EBL) step [20,21] with a reactive ion etching (RIE) and then nanowires with widths ranging from 90 to 150 nm are made. The devices are folded to cover a sensitive squared

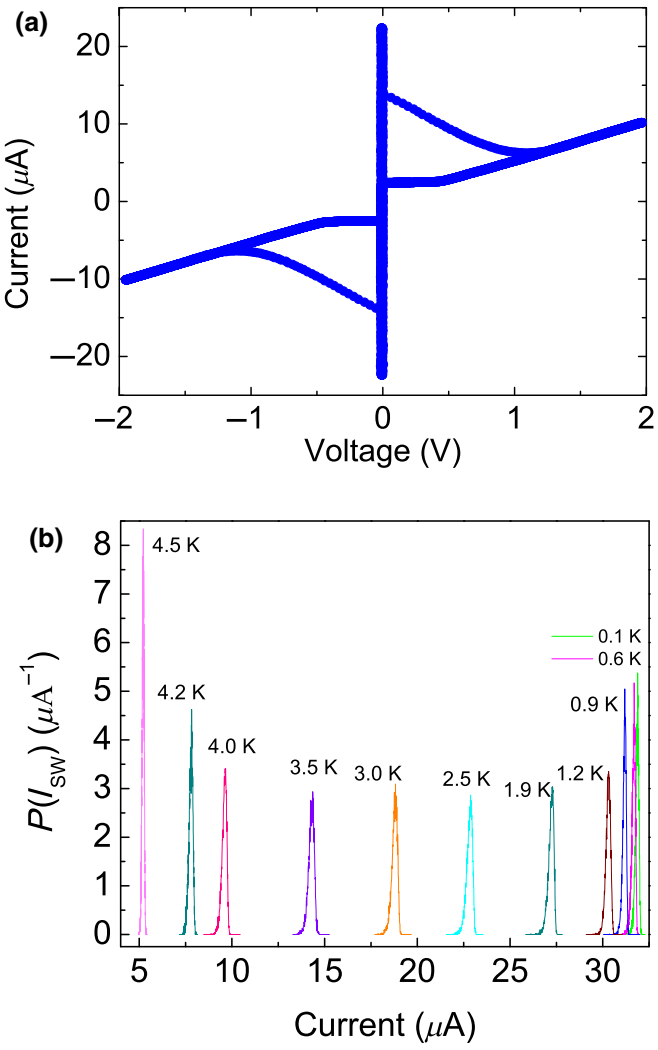

FIG. 1. (a) Current-voltage characteristic of a nanomeander 140 nm wide, measured at $T = 2.5$ K, whihc represents the typical SNSPD operating temperature. In the inset a scanning electron microscope micrograph of a corner of the made meanderlike devices. (b) Measured switching current distributions at different temperatures.

TABLE I. Parameters of the devices studied in this work. R_{square} is the resistance per square.

Device	d (nm)	w (nm)	T_C (K)	$J_{c@T=1K}$ (MA/cm^2)	R_{square} (Ω)	R_N (kΩ)
A	9	90	5.4	0.6	257	172
B	9	140	5.5	2.4	270	180

area of $5 \times 5\mu m^2$ by using a meander geometry. In the inset of Fig. 1(a) a typical characterized nanostructure is shown and its bent side shows a smooth angle designed to avoid the crowding effect at the edges [22]. In the following, we focus on the analysis on two nanomeanders with different widths, 90 nm (sample A) and 140 nm (sample B) wide, respectively.

B. Measurements and experimental observations

Measurements are performed anchoring the samples to the mixing chamber of Oxford Triton Cryogen-free dilution cryostat, with a base temperature of about 10 mK. Various stages of filtering together with details on low-noise electronics used for the experiment are reported elsewhere [23,24]. The current-voltage characteristic of sample B at 2.5 K is shown in Fig. 1(a). As the bias current is swept from zero to higher values the nanowire exhibits an abrupt transition from the superconducting state (zero voltage) to a finite voltage state at the switching current, I_{sw}. The abrupt current suppression is caused by the high normal resistance, R_N, value of the nanomeander ($R_N \sim 300\,k\Omega$), comparable to that of the resistance used in series to the generator (100 kΩ). The nanowire remains in the finite voltage state until the current is reduced below the retrapping current where it returns in the superconducting state. This gives rise to a hysteretic current-voltage characteristic. A similar trend is observed on sample A. At high temperatures (T close to T_c), the hysteresis collapse to zero and the sharp edge in the current-voltage curve turns in a smooth rounding. This behavior is often considered as a footprint of vortex mechanisms [25]. The behavior of the I_c and retrapping current as a function of the temperature is reported in Ref. [26].

In Table I we present the device parameters.

The recording of I_{sw} is repeated 10 000 times at each temperature, ranging from 4.5 K down to 10 mK. At any given temperature, the switching current exhibits a stochastic nature, resulting in a distribution of switching currents, $P(I_{sw})$. To avoid heating effects, which would distort the measurements, the ramp is set in order to reduce the time that the device spends in the resistive state and to increase that passed in the superconducting state. Therefore, the current amplitude ΔI is slightly larger than the critical current and the ramp frequency $1/\Delta t$ is of the order of 10 Hz. We choose different sweep rates, 1000 and 167 μA/s for samples B and A, respectively, because of a different critical current of the devices. $P(I_{sw})$ recorded at different temperatures for sample B is shown in Fig. 1(b). In Fig. 2 we show the standard deviation, σ, of the measured $P(I_{sw})$ for each temperature. We also include the obtained results for NbN and Nb-Ti-N based SNSPDs [16,27], and different regimes are distinctly visible. In general, σ is almost constant at very low temperatures. After that, σ increases with the temperature and finally it exhibits a prominent decrease by increasing temperature. The behavior of the MoSi nanomeanders is very similar to what has been observed in 2D NbN [15], Nb-Ti-N [16], and 1D Al strip, where the switching is attributed to quantum tunneling [28] or thermally excited single phase slips [27,29]. The decrease of σ measured for high temperature is related to switching by multiple phase slips or multiple fluctuation events [16,20]. According to the literature, in the intermediate range of temperatures, a single fluctuation event is by itself energetically sufficient to properly trigger a full superconducting to resistive state transition. In this temperature regime, we calculate the switching rates, Γ, by performing the Kurkijärvi-Fulton-Dunkleberger transformation following Ref. [30]. We observe that Γ decreases exponentially with bias current over about 4 orders of magnitude, as shown in Fig. 2(b). We stress that the calculated Γ also represents the measured dark-count rate and the fluctuation-event rate, whether they are single vortices, vortices pairs, or hotspots.

III. FLUCTUATION EVENTS

Various mechanisms could be considered as responsible for the fluctuation rates measured in our experiments depending on the temperature range considered [10] but we consider just 2D vortex models to give a description of our datasets. Indeed, in MoSi nanomeanders, the coherence length, ξ, and Λ are known to be around 10 nm and 50 μm, respectively [31]. Since in our devices the condition $d \leq \xi \ll w$ is satisfied, the strips can be considered a quasi-two-dimensional system. For this reason, in the following analysis we do not consider 2π-phase slip since the energy barrier for the nucleation of a normal state region becomes relevant in small superconducting wires with a cross-section area approximately ξ^2 [5]. The Likharev condition $w \geq 4.4\xi$ is also satisfied [32], ensuring that the strips are wide enough for nucleation and the propagation of vortices.

In our analysis we particularly focus on the temperature range from 1.0 to 3.0 K, corresponding to T/T_c from 0.2 to 0.5. This is done mainly for two reasons: first, as one can see in Fig. 2(a), in this regime there is a linear dependence of σ on the temperature and a consequent one-to-one correspondence between the fluctuation rate and the switching

rate [16]. Secondly, this is the standard operating temperature of cryogen-free cryostats, typically adopted for SNSPD operations. Therefore, in the following analysis, we exclude fluctuation mechanisms due to quantum tunneling of vortices through the edge barrier, as they become relevant only at sub-Kelvin temperatures and confine our discussion only to the thermal regime [33].

A. Fluctuation models

Vortices can arise in superconducting strips as single vortices (VH) due to an external magnetic field, such as the magnetic self-field generated by the bias current, or as VAPs as topological excitations of a 2D superconducting film.

The activation of the dissipation process requires, due to the boundary conditions, the overcoming of an energy barrier $U(I_b,T)$, which is always guaranteed in this temperature regime by thermal excitations. The rate of dissipative events, which are referred to as fluctuations, may be expressed through the Boltzmann factor as

$$\Gamma(I_b,\ T) = \Omega \exp[-U(I_b,\ T)/k_B T], \tag{1}$$

where Ω and k_B are the attempted frequency and the Boltzmann constant, respectively. The analytic expressions for $U(I_b,T)$ differs depending on the mechanisms.

In the VAP model, the collapse of a long-range order parameter gives rise to the so-called topological defects that, in thin superconducting films, appear as vortices pairs, according to the BKT model [34,35]. Below T_{BKT}, vortices pairs, characterized by a supercurrent circulating in opposite directions, are in a bound VAP state. However, under the condition $w \geq 4.4\xi$ and in the presence of a bias current I_b, a Lorentz force is exerted on VAPs and directed in opposite directions for the vortex and the antivortex, respectively. The resulting torque forces VAPs to align perpendicularly to the current flow. The binding energy changes with the angle and reaches its minimum at $\pi/2$. As shown by Mooji [36], the interplay between the repulsion of vortices in a pair due to the Lorentz force and their magnetic attraction defines the current-dependent $r = 2.6\xi\, I_c/I_b$, leading to the minimal binding energy of the pair U_{VAP}. According to the models in Refs. [10,37], the U_{VAP} is given by

$$U_{\mathrm{VAP}} = \frac{A(T)}{\varepsilon}\left[\ln\left(\frac{2.6I_c(T)}{I_b}\right) - 1 + \frac{I_b}{2.6I_c(T)}\right], \tag{2}$$

where $A(T) = \Phi_0^2/\pi\mu_o\Lambda(T)$ is the vortex activation energy and ε is the averaged polarizability of a VAP within the entire VAP population. We use the conventional notation where Φ_0 is the flux quantum and μ_o the vacuum permeability. The motion of normal core vortices dissipates energy, leading to the formation of a nonsuperconducting domain resulting in a voltage transient.

On the other hand, we also consider the nucleation of single vortices close to the edge of the strip. The probability for thermally activated VH over the energy barrier is again proportional to the Boltzmann factor $\exp[-U_{\mathrm{VH}}/k_B T]$, where U_{VH} is now given by [10]

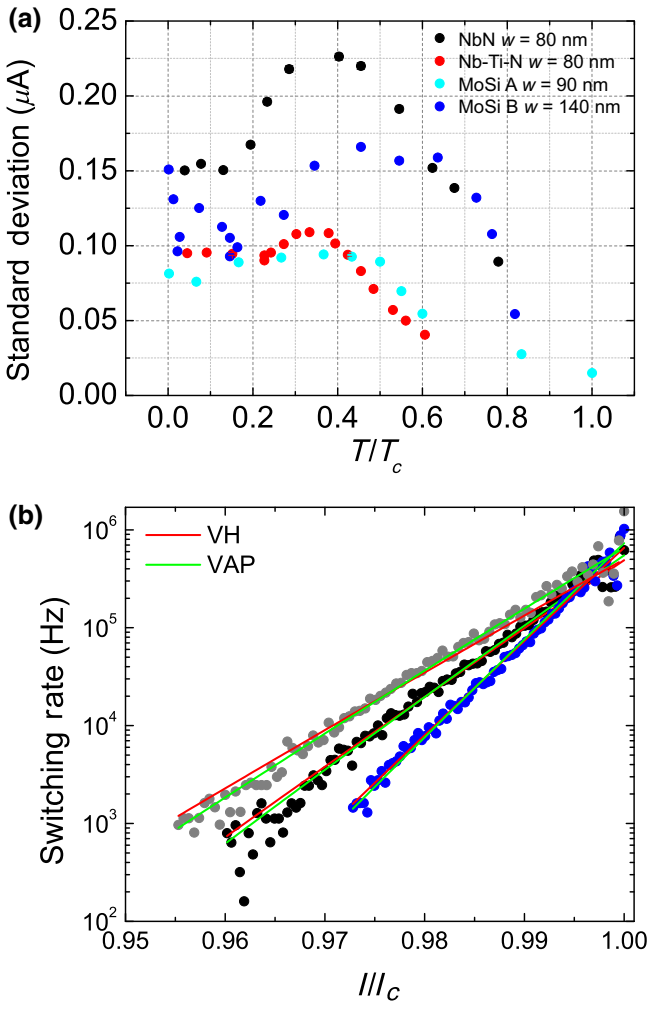

FIG. 2. (a) The standard deviation of $P(I_{\mathrm{sw}})$ as a function of the normalized temperature for the MoSi/Al device A (cyano points) and MoSi/Al device B (blue points), Nb-Ti-N device (red points) and NbN (dark points), respectively [27]. The errors on standard deviation are about 1%. (b) Switching rates versus normalized bias current for three different relative temperatures, T/T_c, of sample B (0.27 blue, 0.35 black, 0.45 green). The solid red and green curves are the fitting curves obtained by using vortex hopping and vortex antivortex pair models, respectively.

$$U_{\mathrm{VH}}(T,\ I_b) = E_B(T,\ I_b)\left[\ln\left(\frac{2w}{\pi\xi(T)}\frac{1}{\sqrt{1+[((\Phi_0 I_b)/(\pi E_B(T,\ I_B)))]^2}}\right) - \frac{\Phi_0 I_b}{\pi E_B(T,\ I_B)}\left(\arctan\left[\frac{\pi E_B(T,\ I_B)}{\Phi_0 I_b}\right] - \frac{\pi\xi(T)}{2w}\right)\right] \tag{3}$$

and the energy scale E_B is

$$E_B(I_b, T) = \frac{{\Phi_0}^2}{2\pi\mu_0\Lambda(I_b, T)} = \frac{A(T)}{2}. \tag{4}$$

Once a vortex jumps over the barrier, the Lorentz force will move it across the strip. As in the VAP scenario, the motion of these free vortices across the strip creates a nonsuperconducting domain.

B. Data analysis

We fit the obtained fluctuation rates, for both samples A and B, by using Eq. (1) with $U(I_b, T)$ represented by Eqs. (2) and (3) in the range of temperatures where only a single event is responsible of the switching. We observe that both VAP and VH models are in good agreement with experimental data; hence, we cannot exclude the presence of both mechanisms. The values of the fitting parameters, $A(T)/\varepsilon$, E_B, and ξ are reported in Table II and they are reasonably close to the ones reported in the literature [38]. Interestingly, in the case of the narrowest nanomeander (sample A) the $A(T)/\varepsilon$ and E_B parameters are about a factor of 5–6 lower than in other devices. The energy barriers U_{VAP} and U_{VH} expressed as a function of the normalized temperature at $I_b/I_c = 0.99$ are reported for all samples in Fig. 3(a), showing a weak dependence on the temperature. One can notice that the binding energy of the VAP and VH is significantly lower in the case of the narrowest wires, thus confirming that the narrowest wires are generally more sensitive.

Inverting Eqs. (2) and (3), we calculate the parameters ε, Λ, while the effective penetration depth in thin film $\lambda(d \ll \lambda)$ is provided by the relation $\lambda^2(T) = d\Lambda(\mathrm{T})/2$. We estimate the coherence length ξ_0 for sample B, equal to 9.3 nm (see Appendix) and according the Ginsburg Landau (GL) theory $\xi_{\mathrm{GL}} = 7.6$ nm from $\xi_{\mathrm{GL}}^2 = \xi_0^2/\sqrt{2}$. This value agrees with the values found in the literature [31] proving the validity of the fitting procedure reported in the Appendix. The obtained ξ_0 values further proves that the 2D approximation is applicable and validates both models.

In Fig. 3(b) we plot the energy barriers, extracted from the fitting procedure, in the unit of k_B for both models as a function of the reduced bias current I_b/I_c for samples A and B at $T/T_c = 0.4$. In the narrower sample A the excitation energies for VAP and VH are comparable to each other, while the single vortices' VH mechanism exhibits a higher barrier with respect to the VAP in the wider sample, thus indicating that the VAP mechanism is favored. We observe that at $I_b/I_c = 0.4$ for sample B, there is a crossover from the VH dominated regime to VAP as the strip width is increased.

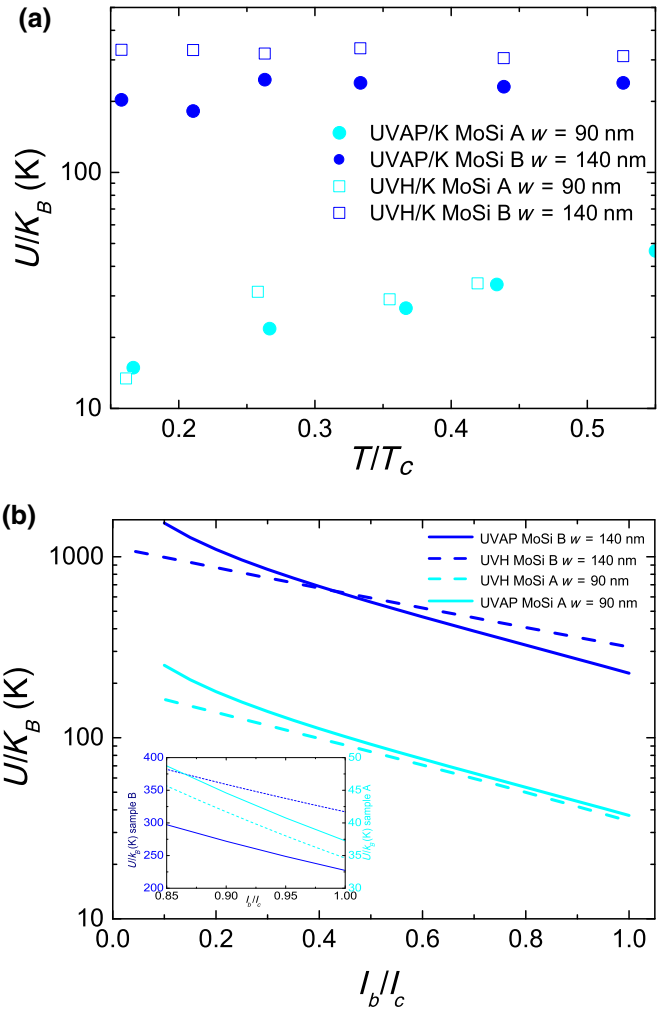

FIG. 3. (a) Estimated energy barriers, in the unit of k_B, at fixed $I_b/I_c = 0.99$ by using VAP (solid circles) and VH (squares) models for nanowires having different widths. (b) Energy barriers in the unit of k_B for both models as a function of the reduced bias current I_b/I_c for samples A and B at $T/T_c = 0.4$. The inset shows the enlargement of the energy barriers at high values of I_b/I_c.

TABLE II. SNSPD parameters determined at $T/T_c = 0.4$. A/ε is obtained by fitting the switching rate data with Eqs. (1) and (2), while ξ and E_B are attained by fitting the escape rate data with Eqs. (1)–(3). Using $A = 2\,E_B$, the polarizability ε is also calculated while λ and Λ are computed by Eq. (4).

			A/ε (meV)	ξ (nm)	E_B (meV)	ε	λ (nm)	Λ (μm)
Sample	w (nm)	d (nm)	VAP model fitting parameter	VH model fitting parameter		Calculated parameters		
A	90	9	9.42	13	11.1	2.36	1168	303
B	140	9	57.46	15	55	1.91	525	61
NbN[a]	175	8	105.26	4.5	340	1.9	368	34
Nb-Ti-N[b]]	80	5	41.16	15	52	2.5	404	65

[a]Ref. [34]
[b]Ref. [14]

The rate of single vortices entering depends on the length L of the strip whereas the rate of VAP breakup depends on the area (Lw) of the superconducting film [10,11]. Therefore, the ratio of VAP to VH rates in meandered lines is supposed to depend on the strip width w and one can hence expect that VAP events start to dominate in wider strips. In our case this ratio effectively increases as a function of the width of the strip and the VAPs present a lower energy barrier in the high-bias-current region, indicating that this process occurs with higher probability.

IV. COMPARISON WITH OTHER MATERIALS AND EXPERIMENTAL OUTCOMES

Based on the performed analysis, in order to underline the role that each material and its sizes play in the studied vortex dynamic, we also compare the results obtained on MoSi/Al nanomeanders with similar realized with niobium-based superconducting materials, typically adopted for SNSPD fabrication such as NbN, Nb-Ti-N [16,38]. For this purpose, we analyze the switching current distributions of all the devices and estimate the energy barriers in the case of VAP and VH mechanisms. As observed in Fig. 2(a), for similar widths, the MoSi/Al SNSPD shows fluctuations comparable to those observed for the Nb-Ti-N [16] and lower than that of NbN [38].

We follow the same procedure described above for the switching current distribution analysis and we plot the energy barrier at a fixed T/T_c ratio for MoSi/Al, NbN, and Nb-Ti-N SNSPDs with comparable widths. From those plots (Fig. 4) it is possible to observe that the energy barriers are lower in MoSi/Al, both at fixed temperature and geometries. This confirms the experimental well-known result that this material exhibits higher dark-count rates. However, this can also be considered a sign of higher sensitivity to lower-energy excitations [31]. By using the hotspot model [6], it is possible to estimate the maximum detectable radiation wavelength $\lambda_{\max} = hc/E_{\min} \cong 12$ μm and the minimum detectable energy $E_{\min} = 103$ meV for a 100-nm-wide and 5-nm-thick nanomeander based on MoSi/Al. The energy and wavelength values can be compared with what is obtained for other materials such as NbN, and a NbRe nanomeanders with the same widths and thicknesses. By using the parameters reported in Ref. [39] we find $E_{\min} = 584$ meV and $\lambda_{\max} \cong 2$ μm and $E_{\min} = 19$ meV and $\lambda_{\max} \cong 64$ μm, for NbN and NbRe, respectively. However, in photoresponse experiments based on NbN nanomeander, wavelengths up to 5 μm have been detected, although with poor efficiency for Ref. [40] and this result cannot be predicted according with the simple hotspot model.

In a vortice-assisted detection mechanism scenario, which ascribes the hotspot formation to the movement of vortices across the strip [10], the energy scales to be considered are U_{VAP} or U_{VH}. From the values calculated, an average estimation of $U \cong 20$ and $U \cong 40$ meV for MoSi/Al and NbN nanowire provides maximum detectable wavelengths of $\lambda \sim 60$ and $\lambda \sim 30\,\mu$m, respectively, without considering losses due to the coupling between the device and the optical source. These results favor a vortex-based detection model. Moreover, we prove that the switching current distributions are a powerful tool to estimate the SNSPD detection limits, and this method is easier compared to the techniques required to estimate the diffusivity, the thermalization time, the superconducting gap, and the density of states at the Fermi level.

The values obtained indicate that the SNSPD based on MoSi/Al are more suitable than the typically used NbN and Nb-Ti-N to detect infrared and midinfrared photons since the energetic barrier is lower. Besides a deeper understanding of the physics of these devices, there are some interesting implications under the applicative point of view. The first one is that the longest detectable wavelengths obtained here are even longer that what is expected by the predictions of the hotspot model [6]. This can be a very interesting result in Lidar applications for atmospheric aerosols since working in the infrared and midinfrared range in single-photon counting regime would different pollutants species and size to be distinguished [41,42]. The last point is especially relevant to monitor

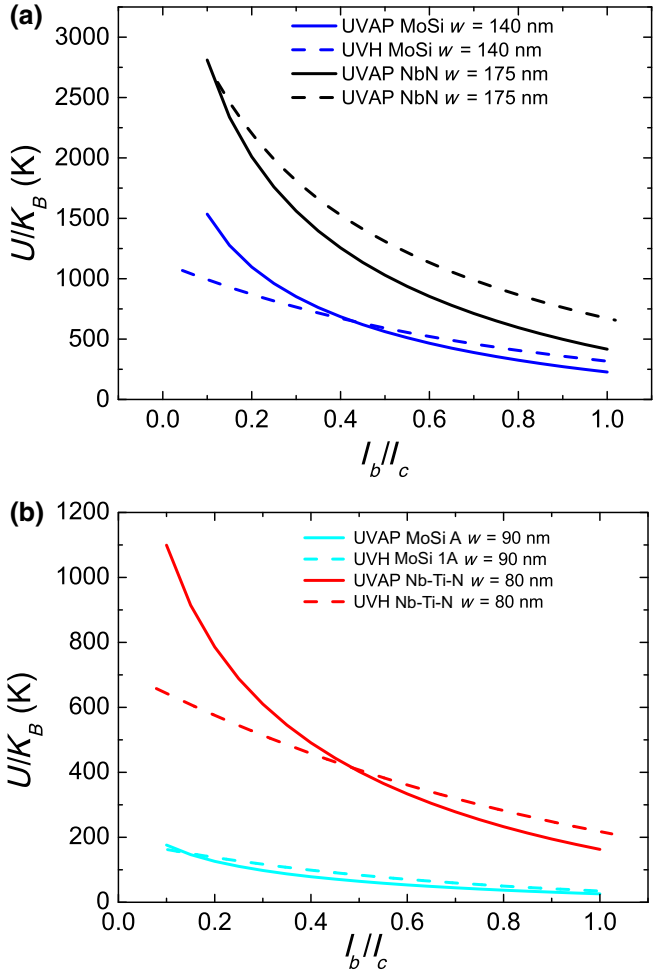

FIG. 4. Energy scale normalized to Boltzmann constant as a function of the bias current at $T/T_c = 0.4$ for different materials (blue and cyan lines MoSi device, black lines NbN, and red lines Nb-Ti-N) and width of the strips: (a) 140 and 175 nm; (b) 80 and 90 nm, respectively.

the air quality, but the resolution provided by the Lidar is limited at the moment by the source, optics, and detector limitations on the operating wavelength. The second implication can be better understood looking at Fig. 3(a). It shows that in wider SNSPD the energy barriers remain almost constant as the temperature changes and the dark-count rate can be lower with respect to narrower nanowires. This aspect could be very promising for the use of SNSPD for dark-matter detection where large areas are required [43]. Finally, experimental data supporting the perspective of working in the midinfrared with high-efficiency single-photon detectors. In particular, high-sensitivity molecular spectroscopy can access the wavelength range where fingerprint of molecular absorption occurs. Recently, tunable midinfrared lasers are being developed [44] and a combination of this technology with the performance of SNSPDs represents very solid foundation for future innovation.

V. CONCLUSIONS

In this work we study 9-nm-thick MoSi SNSPDs covered with a very thin (2 nm) layer of aluminum by measuring the switching current distributions in a wide range of temperatures from 4.2 K down to 10 mK. The switching current distributions measurements give us the possibility to explore the role of vortices in dark-count generation in SNSPDs made of different materials and geometries. In the framework of both the VAP and VH models we evaluate the excitation energies and we find that for the narrowest strips they are comparable while the VAP mechanism is favored in wider devices. We compare the energy scales of MoSi/Al, NbN and Nb-Ti-N and the lower excitation energies observed in MoSi/Al nanowires explain the peculiarity of this material to work at longer wavelengths with higher quantum-detection efficiency. In the scenario of the hotspot model, we calculate the maximum detectable wavelength and confirm the prospective to work up to $\lambda_{\max} \cong 12$ μm with MoSi-based SNSPD. This limit could be even higher in the framework of a vortex-based detection model. We believe that a single-photon detector with the performance of a SNSPD up to 12 μm and beyond would be enabling technology for fundamental science and commercial applications.

ACKNOWLEDGMENTS

This work is carried out in the context of OT4CLIMA project, funded by the Italian Ministry of Education, University and Research, within the PON 2014-2020 Industrial Research program. The activities have received funding from the European Unions Horizon 2020 research and innovation programme under Grant Agreement No. 654109, ACTRIS2 project.

APPENDIX

The coherence length ξ_0 is estimated by using the following analytical expression:

$$\xi^2(T/T_C) = \frac{\xi_0^2}{(1 - T/T_C)} \frac{1}{\sqrt{1 + T/T_C}}. \qquad \text{(A1)}$$

We find for sample B, $\xi_0 = 9.3$ nm and $\xi_{GL} = 7.6$ nm from $\xi_{GL}^2 = \xi_0^2/\sqrt{2}$. The GL coherence length determined by the fitting procedures, as shown in Fig. 5, is used to estimate the fundamental material parameters of our MoSi samples such as the electrons' diffusion constant $D = 0.43$ cm^2/s and the density of states at the Fermi level $N(0) = 54\ 10^{21}$ eV^{-1} cm^{-3} by using $D = \xi^2(0)\Delta(0)/\hbar$, $\Delta(0) = 1.76\, k_B T_c$ and $N(0) = 1/e^2 \rho_N D$, while the electrons thermalization time τ_{th} is assumed to be 10 ps [34].

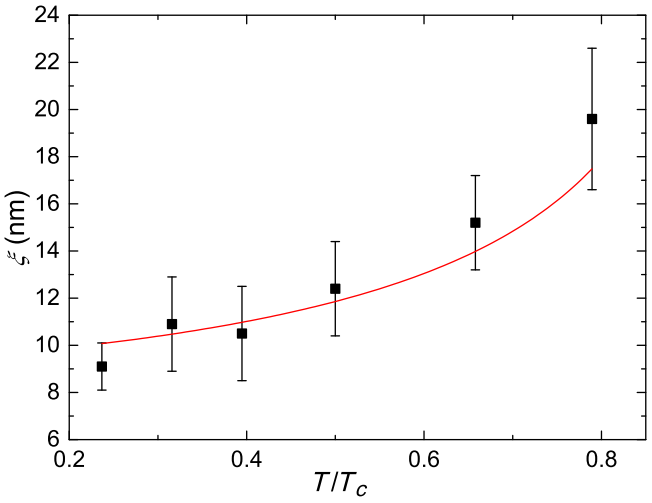

FIG. 5. Behavior of the ξ value, extracted from the fitting of experimental data by the VH model [Eq. (3)], as a function of the temperature for sample B.

[1] G. N. Gol'tsman, O. Okunev, G. Chulkova, A. Lipatov, A. Semenov, K. Smirnov, B. Voronov, A. Dzardanov, C. Williams, and Roman Sobolewski, Picosecond superconducting single-photon optical detector, Appl. Phys. Lett. **79**, 705 (2001).

[2] Y. Lixing, Superconducting nanowire single-photon detectors for quantum information, Nanophotonics **9**, 2673 (2020).

[3] I. E. Zadeh, J. Chang, J. W. N. Los, S. Gyger, A. W. Elshaari, S. Steinhauer, S. N. Dorenbos, and Val Zwiller, Superconducting nanowire single-photon detectors: A perspective on evolution, state-of-the-art, future developments, and applications, Appl. Phys. Lett. **118**, 190502 (2021).

[4] D. Salvoni, A. Boselli, A. Sannino, L. Parlato, M. Ejrnaes, C. Zhang, L. You, X. Wang, S. Amoruso, and G. P. Pepe, Demonstration of atmospheric Lidar measurement in the infrared wavelength domain with a superconducting nanowire single photon detector, Chem. Eng. Trans. **84**, 175 (2021).

[5] A. Engel, J. J. Renema, K. Il'in, and A. Semenov, Detection mechanism of superconducting nanowiresingle-photon detectors, Supercond. Sci. Technol. **28**, 114003 (2015).

[6] A. Semenov, A. Engel, H. Hübers, K. Il'in, and M. Siegel, Spectral cut-off in the efficiency of the resistive state formation caused by absorption of a single-photon in current-carrying superconducting nano-strips, Eur. Phys. J. B **47**, 495 (2005).

[7] F. Mattioli, R. Leoni, A. Gaggero, M. G. Castellano, P. Carelli, F. Marsili, and A. Fiore, Electrical characterization of superconducting single-photon detectors, J. Appl. Phys **101**, 054302 (2007).

[8] D. Y. Vodolazov, Single-Photon Detection by a Dirty Current-Carrying Superconducting Strip Based on the Kinetic-Equation Approach, Phys. Rev. Appl. **7**, 034014 (2017).

[9] Yu. P. Korneeva, D. Y. Vodolazov, A. V. Semenov, I. N. Florya, N. Simonov, E. Baeva, and A. A. Korneev, Optical Single-Photon Detection in Micrometer-Scale NbN Bridges, Phys. Rev. Appl. **9**, 064037 (2018).

[10] H. Bartolf, A. Engel, A. Schilling, K. Il'in, M. Siegel, H. W. Hübers, and A. Semenov, Current-assisted thermally activated flux liberation in ultrathin nanopatterned NbN superconducting meander structures, Phys. Rev. B **81**, 024502 (2010).

[11] L. N. Bulaevskii, M. J. Graf, C. D. Batista, and V. G. Kogan, Vortex-induced dissipation in narrow current-biased thin-film superconducting strips, Phys. Rev. B **83**, 144526 (2011).

[12] D. Y. Vodolazov, Y. P. Korneeva, A. V. Semenov, A. A. Korneev, and G. N. Goltsman, Vortex-assisted mechanism of photon counting in a superconducting nanowire single-photon detector revealed by external magnetic field, Phys. Rev. B **92**, 104503 (2015).

[13] Y. Liu, D. B. Haviland, L. I. Glazman, and A. M. Goldman, Resistive Transitions in Ultrathin Superconducting Films: Possible Evidence for Quantum Tunneling of Vortices, Phys. Rev. Lett. **68**, 2224 (1992).

[14] D. Massarotti, L. Longobardi, L. Galletti, D. Stornaiuolo, D. Montemurro, G. Pepe, G. Rotoli, A. Barone, and F. Tafuri, Escape dynamics in moderately damped Josephson junctions, Low Temp. Phys. **38**, 263 (2012).

[15] A. Murphy, A. Semenov, A. Korneev, Y. Korneeva, G. Gol'tsman, and A. Bezryadin, Three temperature regimes in superconducting photon detectors: Quantum, thermal and multiple phase-slips as generators of dark counts, Sci. Rep. **5**, 10174 (2015).

[16] M. Ejrnaes, D. Salvoni, L. Parlato, D. Massarotti, R. Caruso, F. Tafuri, X. Y. Yang, L. X. You, Z. Wang, G. P. Pepe, and R. Cristiano, Superconductor to resistive state switching by multiple fluctuation events in NbTiN nanostrips, Sci. Rep. **9**, 1 (2019).

[17] D. Salvoni, L. Parlato, M. Ejrnaes, F. Mattioli, A. Gaggero, F. Martini, A. Ausanio, D. Massarotti, D. Montemurro, H. G. Ahmad, *et al.*, Demonstration of single photon detection in amorphous molybdenum silicide/aluminium superconducting nanostrip, IEEE Instr. Meas. Mag. **24**, 69 (2021).

[18] S. S. Ustavschikov, M Yu Levichev, I Yu Pashenkin, A. M. Klushin, and D Yu Vodolazov, Approaching depairing current in dirty thin superconducting strip covered by low resistive normal metal, Supercond. Sci. Technol. **34**, 015004 (2021).

[19] N. O. Simonov, Y. Koorneva, and A. Koornev, Enhance of the superconducting properties of the NbN/Au bilayer bridges, J. Phys.: Conf. Ser. **1695**, 012132 (2020).

[20] F. Martini, A. Gaggero, F. Mattioli, and R. Leoni, Single photon detection with superconducting nanowires on crystalline silicon carbide, Opt. Express **27**, 29669 (2019).

[21] G. Kunakova, A. P. Surendran, D. Montemurro, M. Salvato, D. Golubev, J. Andzane, D. Erts, T. Bauch, and F. Lombardi, Topological insulator nanoribbon Josephson junctions: Evidence for size effects in transport properties, J. Appl. Phys. **128**, 194304 (2020).

[22] J. R. Clem and K. K. Berggren, Geometry-dependent critical currents in superconducting nanocircuits, Phys. Rev. B **84**, 174510 (2011).

[23] L. Parlato, R. Caruso, A. Vettoliere, R. Satariano, H. G. Ahmad, A. Miano, D. Montemurro, D. Salvoni, G. Ausanio, F. Tafuri, G. P. Pepe, D. Massarotti, and C. Granata, Characterization of scalable Josephson memory element containing a strong ferromagnet, J. Appl. Phys. **127**, 193901 (2020).

[24] H. G. Ahmad, R. Caruso, A. Pal, G. Rotoli, G. P. Pepe, M. Blamire, F. Tafuri, and D. Massarotti, Electrodynamics of Highly Spin-Polarized Tunnel Josephson Junctions, Phys. Rev. Appl. **13**, 014017 (2020).

[25] J. Kitaygorsky, I. Komissarov, A. Jukna, D. Pan, O. Minaeva, N. Kaurova, A. Divochiy, A. Korneev, M. Tarkhov, B. Voronov, and I. Milostnaya, Dark counts in nanostructured NbN superconducting single-photon detectors and bridges, IEEE Trans. Appl. Superc. **17**, 275 (2007).

[26] L. Parlato, D. Salvoni, H. G. Ahmad, D. Massarotti, D. Montemurro, R. Ferraiuolo, L. di Palma, R. Satariano, F. Tafuri, G. P. Pepe, *et al.*, in *IEEE 14th Workshop on Low Temperature Electronics, WOLTE 2021 – Proceedings*, Volume 2021 (2021).

[27] L. Parlato, D. Salvoni, M. Ejrnaes, D. Massarotti, R. Caruso, R. Satariano, F. Tafuri, X. Y. Yang, L. You, Z. Wang, *et al.*, The role of multiple fluctuation events in NbN and NbTiN superconducting nanostrip single-photon detectors, J. Low Temp. Phys. **199**, 1 (2020).

[28] M. Singh and M. H. W. Chan, Observation of individual macroscopic quantum tunneling events in superconducting nanowires, Phys. Rev. B **88**, 064511 (2013).

[29] P. Li, Switching Currents Limited by Single Phase Slips in One-Dimensional Superconducting Al Nanowires, Phys. Rev. Lett. **107**, 137004 (2011).

[30] T. A. Fulton and L. N. Dunkleberger, Lifetime of the zero-voltage state in Josephson tunnel junctions, Phys. Rev. B **9**, 4760 (1974).

[31] Yu. P. Korneeva, N. N. Manova, I. N. Florya, M. Yu. Mikhailov, O. V. Dobrovolskiy, A. A. Korneev, and D. Yu. Vodolazov, Different Single-Photon Response of Wide and Narrow Superconducting $MoxSi_{1-x}$ Strips, Phys. Rev. Appl. **13**, 024011 (2020).

[32] C. Qiu and T. Qian, Numerical study of the phase slip in two-dimensional superconducting strips, Phys. Rev. B **77**, 174517 (2008).

[33] E. Trabaldo, S. Ruffieux, E. Andersson, R. Arpaia, D. Montemurro, J. F. Schneiderman, A. Kalaboukhov, D. Winkler, F. Lombardi, and T. Bauch, Properties of grooved Dayem bridge based $YBa_2Cu_3O_{7-\delta}$ superconducting quantum interference devices and magnetometers, Appl. Phys. Lett. **116**, 132601 (2020).

[34] Z. L. Berezinskii, Destruction of long-range order in one-dimensional and two-dimensional systems having a continuous symmetry group 1. Classical systems, Zh. Eksp. Teor. Fiz. **59**, 907 (1970).

[35] J. M. Kosterlitz and D. J. Thouless, Ordering, metastability and phase transitions in two-dimensional systems, J. Phys. C **6**, 1181 (1973).

[36] J. E. Mooij, in *NATO ASI, Series B*, edited by A. M. Goldman, S. A. Wolf (Plenum, New York, 1984), Vol. 109, p. 325.

[37] A. Engel, A. D. Semenov, H.-W. Hübers, K. Il'in, and M. Siegel, Fluctuation effects in superconducting nanostrips, Physica C **444**, 12 (2006).

[38] U. Nasti, L. Parlato, M. Ejrnaes, R. Cristiano, T. Taino, H. Myoren, R. Sobolewski, and G. P. Pepe, Thermal fluctuations in superconductor/ferromagnet nanostripes, Phys. Rev. B **92**, 014501 (2015).

[39] C. Cirillo, J. Chang, M. Caputo, J. W. N. Los, S. Dorenbos, I. Esmaeil Zadeh, and C. Attanasio, Superconducting nanowire single photon detectors based on disordered NbRe films, Appl. Phys. Lett. **117**, 172602 (2020).

[40] F. Marsili, F. Bellei, F. Najafi, A. E. Dane, E. A. Dauler, R. J. Molnar, and K. K. Berggren, Efficient single photon detection from 500 nm to 5 μm wavelength, Nano Lett. **12**, 4799 (2012).

[41] A. Sorrentino, A. Sannino, N. Spinelli, M. Piana, A. Boselli, V. Tontodonato, P. Castellano, and X. Wang, A Bayesian parametric approach to the retrieval of the atmospheric number size distribution from lidar data, Atmospheric Measurement Techniques **15**, 149 (2022).

[42] D. Salvoni, M. Ejrnaes, L. Parlato, A. Sannino, A. Boselli, G. P. Pepe, R. Cristiano, and X. Wang, Lidar techniques for a SNSPD-based measurement, J. Phys.: Conf. Series **1182**, 012014 (2019).

[43] Y. Hochberg, I. Charaev, S. W. Nam, V. Verma, M. Colangelo, and K. K. Berggren, Detecting Sub-GeV Dark Matter with Superconducting Nanowires, Phys. Rev. Lett. **123**, 151802 (2019).

[44] B. G. Lee, M. A. Belkin, R. Audet, J. MacArthur, L. Diehl, C. Pflügl, F. Capasso, D. C. Oakley, D. Chapman, A. Napoleone, and D. Bour, Widely tunable single-mode quantum cascade laser source for mid-infrared spectroscopy, Appl. Phys. Lett. **91**, 231101 (2007).